

# **Surfactant adsorption kinetics by total internal reflection Raman spectroscopy. Part I: pure surfactants on silica**

David A. Woods,<sup>†</sup> Jordan Petkov,<sup>‡</sup> and Colin D. Bain<sup>\*,†</sup>

*Durham University, Department of Chemistry, University Science Laboratories, South Road, Durham, UK, DH1 3LE, and Unilever Research and Development Laboratory, Port Sunlight, Quarry Road East, Bebington, Wirral, U.K.*

E-mail: c.d.bain@durham.ac.uk

---

\*To whom correspondence should be addressed

<sup>†</sup>Durham University, Department of Chemistry, University Science Laboratories, South Road, Durham, UK, DH1 3LE

<sup>‡</sup>Unilever Research and Development Laboratory, Port Sunlight, Quarry Road East, Bebington, Wirral, U.K.

## Abstract

Total Internal Reflection Raman spectroscopy provides a sensitive probe of surfactants adsorbed at an interface. A visible laser passes through a silica hemisphere and reflects off the flat silica-water interface. An evanescent wave probes  $\sim 100$  nm of solution below the surface and the Raman scattering from this region provides chemically specific information on the molecules present. Here we look at both equilibrium and kinetic aspects of the adsorption of the cationic surfactant cetyltrimethylammonium bromide (CTAB) and the non-ionic surfactant Triton X-100 in single component systems. We use the well-defined wall jet geometry to provide known hydrodynamics for the adsorption process. The well-defined hydrodynamics allows us to model the mass transport of surfactant to the surface which is coupled with a kinetic model consistent with the Frumkin isotherm to produce a complete model of the adsorption process. The fit between this model and the experimental results provides insight into the interactions on the surface.

## Introduction

The kinetics of surfactant adsorption at the solid-water interface plays a central role in a wide-range of practical applications of surfactants. Examples include the wetting of fabrics in detergency,<sup>1</sup> the spreading of agricultural sprays on leaves,<sup>2</sup> the adsorption of collectors on ore particles<sup>3</sup> and the deposition of conditioners on hair and textiles.<sup>4</sup> Classical methods for measuring adsorption isotherms on powders, based on the depletion of surfactant in solution, are not readily extendable to kinetic measurements other than on very long timescales (minutes). Penetration experiments into fibers or packed beds can be carried out on shorter timescales, but are largely of comparative little benefit since it is difficult to relate the penetration rate to a microscopic kinetic model. Quantitative studies therefore tend to use model systems in which adsorption occurs at planar interface that can be interrogated with optical or electrochemical techniques. Cell designs with well-defined hydrodynamics (such as the channel-flow cell or wall jet) then permit quantitative modeling of adsorption kinetics. The closely related techniques of ellipsometry and reflectometry have been

extensively used to study adsorption of single surfactants onto hydrophilic and hydrophobic silica surfaces. These optical techniques have high sensitivity ( $< 1\%$  of a monolayer) and rapid acquisition times (milliseconds) and are well-suited for studying adsorption at the solid-liquid interface, which in most studies takes place on timescales from seconds to minutes depending on whether mass transport or interfacial kinetics limit the adsorption rate. These techniques essentially measure the amount of adsorbed material and provide little or no information on the chemical nature of the adsorbed species.

Practical formulations invariably contain multiple ingredients that are added for a diverse range of purposes, for example to control rheology, disperse particulates, inhibit corrosion or oxidation and prevent bacterial growth. These additives are frequently surface-active. In addition, mixtures of surfactants are frequently employed to improve the effectiveness or efficiency of a formulation. To understand the mode of action of surfactants in mixtures one needs analytical techniques that have chemical as well as interfacial selectivity. ATR-IR is a spectroscopic technique that can be used to study surfactant adsorption kinetics,<sup>5,6</sup> however, it does have significant limitations. The strong IR water band necessitates the use of either deuterated surfactant or solvent to be able to see the comparatively weak hydrocarbon signal. A large sampling area is required to be able to record spectra rapidly, requiring hydrodynamic control over a large region (Clark and Ducker solved this problem elegantly by using a small bubble between incoming and outgoing solutions to force a rapid exchange). Finally, the penetration depth of the IR radiation into the solution varies strongly with IR wavelength, complicating the data analysis. Neutron reflectivity (NR) has been widely used to study pure and mixed layers at solid-liquid interface and is especially valuable for providing insight into surface structure. Acquisition times are typically tens of minutes to hours, which is too slow for most kinetic processes of surfactants at surfaces. Only a limited range of substrates are compatible with NR, of which silicon, quartz and sapphire are the most prevalent,<sup>7</sup> although the range of surfaces can be increased by functionalizing the basic substrate.<sup>8</sup> Chemical specificity in NR normally requires selective deuteration of surfactants.

Total internal reflection (TIR) Raman scattering shares the advantages of ATR-IR in having

chemical selectivity, wide applicability to all molecular species, and surface selectivity through evanescent wave excitation. It has the advantages over ATR-IR that the penetration depth is wavelength independent and generally smaller than in ATR-IR, and that water is a weak Raman scatterer. Raman scattering does, however, have a reputation as being a very weak effect and as a consequence surface-plasmon enhanced Raman scattering (SERS) is almost invariably used when studying surfaces by Raman scattering. Nevertheless, if care is taken to exclude background fluorescence, it is possible to obtain monolayer sensitivity in TIR-Raman scattering without enhancing the electric fields with surface plasmons or the scattering cross-section by resonance with electronic transitions. Since the first demonstration almost 40 years ago,<sup>9</sup> TIR-Raman scattering has been used intermittently to study thin films at air-water, oil-water, solid-water and solid-solid interfaces.<sup>3,10</sup> Recently, we used TIR-Raman scattering to study the adsorption of the cationic surfactant CTAB (hexadecyltrimethylammonium bromide) at the silica-water interface<sup>11</sup> and demonstrated that a sensitivity of 1% of the saturation coverage was achievable ( $\sim 3 \times 10^{-8} \text{ mol m}^{-2}$ ). We now turn our attention to adsorption kinetics. In this paper (Part I), we report the adsorption kinetics of single surfactant systems at the silica-water interface in the controlled environment of a wall jet cell. CTAB and the non-ionic surfactant Triton X-100 (TX-100) are used as exemplars. We demonstrate a time resolution of 2 s with a typical precision of  $1 \times 10^{-7} \text{ mol m}^{-2}$  in the adsorbed amount. In the following paper (Part II), we address the competitive adsorption of CTAB and TX-100 and demonstrate that the same sensitivity and time resolution is achievable in a mixed surfactant system without the use of deuterated surfactants.

The principles of TIR-Raman scattering at the solid-water interface are illustrated in Figure 1. A laser beam is incident at the interface between a transparent solid and an aqueous surfactant solution at an angle above the critical angle for total internal reflection. Although there is no transmitted wave, there is nevertheless an electric field in the water which decays away exponentially with distance from the surface. The decay length (or penetration depth,  $d_p$ ) of the electric field depends on the angle of incidence and the optical properties of the two media but in our experiments is around 200 nm. Since Raman scattering is a linear spectroscopy, the Raman signal is propor-

tional to the intensity of the pump laser and hence to the electric field squared; consequently the effective sampling depth of the TIR-Raman experiments is half of the penetration depth, or around 100 nm in our experiments. Although the electric field is at a maximum at the interface, where the adsorbed surfactant is to be found, surfactant molecules in bulk solution within the evanescent wave are also detected. At concentrations below 1 mM, the bulk contribution to the Raman signal can normally be neglected: in a 1 mM solution there are only  $10^{-7}$  mol m $^{-2}$  of surfactant with a sampling depth of 100 nm. At higher concentrations one has to allow for the bulk contribution, which can be evaluated from measurements well above the critical micelle concentration where the surface concentration is constant.

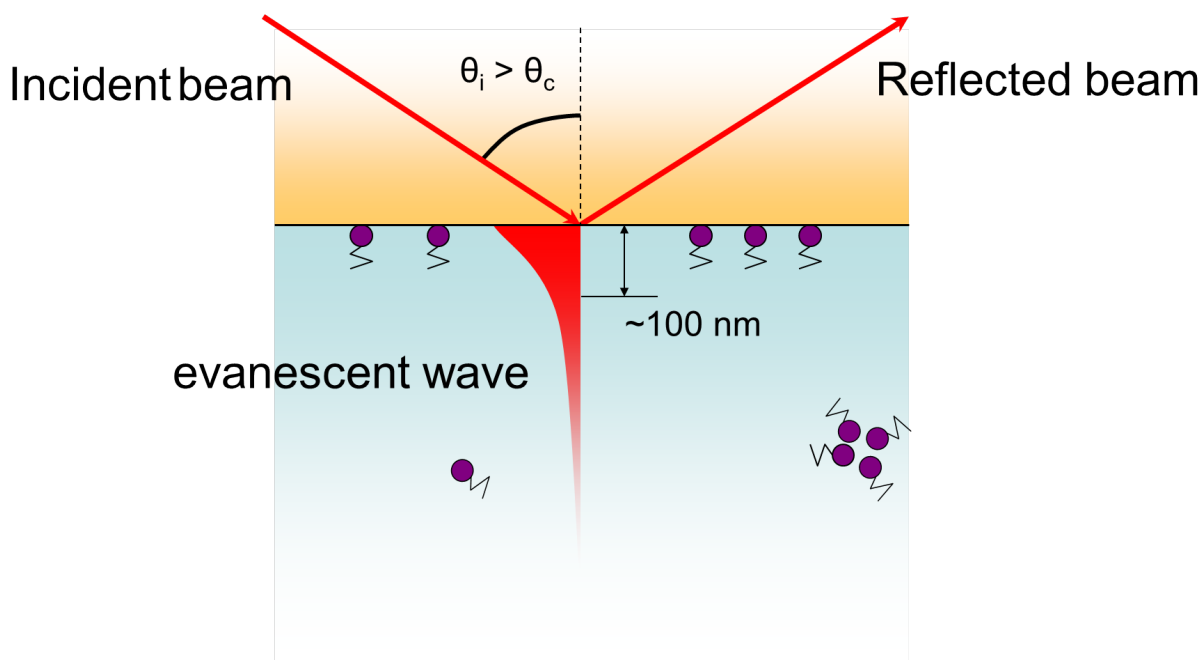


Figure 1: Schematic illustration of a TIR-Raman experiment. The Raman scattered light is collected through the incident medium.

In order to model surfactant adsorption kinetics quantitatively, one needs to have well-defined hydrodynamics.<sup>12–14</sup> For this work we have adopted a well-established approach known as a wall jet<sup>12,15–22</sup> in which the liquid is introduced through a capillary that is placed a short distance from a planar surface aligned perpendicular to the axis of the capillary (see Figure 2). The convective-diffusion equation reduces to a one-dimensional mass transport equation on the axis of the capil-

lary.<sup>23</sup> Provided that the diameter of the laser spot ( $\sim 20 \mu\text{m}$  in our experiments) is much smaller than the diameter of the capillary ( $\sim 2 \text{mm}$ ), this geometry greatly simplifies the theoretical modeling.

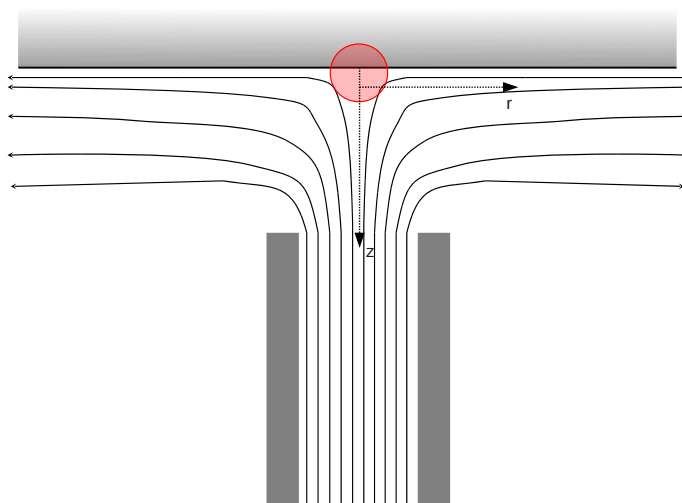


Figure 2: Schematic diagram of streamlines in a wall jet. The analysis region is circled. The wall jet is axisymmetric around the  $z$  axis.

This paper is structured as follows. Section 2 describes the experimental design, the Raman spectra of the pure compounds and the chemometric methods used to analyze the sets of kinetic spectra. Section 3 describes the mass transport model employed. Section 4 presents the equilibrium isotherms of the two surfactants and the best fits to the Frumkin adsorption model. Section 5 presents kinetics of adsorption and desorption of CTAB and TX-100 together with a quantitative analysis of these data. Section 6 concludes with a discussion of the strengths and limitations of the TIR-Raman technique and of the models employed to describe the adsorption kinetics of CTAB and TX-100.

# Experimental

## Materials

Hexadecyltrimethylammonium bromide (CTAB, Sigma-Aldrich, 99%) was recrystallized three times from acetone/methanol. Triton X-100 (TX-100, Sigma-Aldrich) was used as received. Water was obtained from a Millipore Gradient A-10 filtration unit (18.2 M $\Omega$  cm, TOC < 4 ppb). The 10-mm diameter fused silica hemispheres (scratch/dig ratio 40/20) were obtained from Global Optics (Bournemouth, UK).

## Raman spectroscopy

The TIR-Raman system has been described in ref. 11. The Raman light is collected with commercial Raman microscope (Ramascope 1000, Renishaw, Wootton-under-edge, UK). The pump laser is a continuous-wave, frequency-doubled solid-state laser (Opus 532, Laser Quantum, Manchester, UK) with a wavelength of 532 nm. The laser was typically operated at 1.5 W, yielding  $\sim 1.0$  W at sample. The beam was gently focused to a diameter of  $\sim 10$   $\mu$ m. A silica hemisphere was used to minimize optical aberrations. The angle of incidence at the silica-water interface was 73.0 $^\circ$  giving an illuminated region of  $30 \times 10$   $\mu$ m, a penetration depth for the electric field  $d_p = 206$  nm and a sampling depth for Raman scattering of  $d_p/2 = 103$  nm. The incident laser was S polarized (perpendicular to the plane of incidence), since this polarization gave the highest signal levels. The Raman scattered radiation was collected through the fused silica prism with a  $50\times$  ULWD, 0.55 NA objective (Olympus) and directed into the spectrometer. Data were acquired over a fixed wavenumber range encompassing the CH stretching region (from 2600 to 3200  $\text{cm}^{-1}$ ) of the Stokes scattering.

For measurements on equilibrium systems, a typical acquisition consisted of ten co-added scans of 30 s each. Figure 3 (a) shows the raw spectra of the two surfactants and is dominated by the O-H stretching mode of the water in the evanescent wave: even though the Raman scattering cross-section of the O-H bond is much smaller than the C-H bond, there are many more water

molecules than surfactant molecules within the evanescent field. Figure 3 (b) shows the surfactant spectra after subtraction of the water background. The main spectral features in the CTAB spectra (red, dashed line) are the symmetric and antisymmetric methylene stretches at 2852 and 2890  $\text{cm}^{-1}$  respectively, the Fermi resonance of the symmetric stretch with the  $\text{CH}_2$  scissoring mode at 2928  $\text{cm}^{-1}$ ,<sup>24</sup> the asymmetric methyl stretch at 2960  $\text{cm}^{-1}$ , the symmetric methyl stretch from the trimethylammonium headgroups at 2985  $\text{cm}^{-1}$  and the corresponding asymmetric stretch at 3040  $\text{cm}^{-1}$ .<sup>25</sup> The small peak at 2700  $\text{cm}^{-1}$  is the overtone of a C-H bending mode. TX-100 is a nonylphenyl ethoxylate with 9–10 ethylene oxide (EO) groups on average. The Raman spectrum of TX-100 shows a broad and relatively featureless band between 2800 and 3000  $\text{cm}^{-1}$  arising from the CH stretches of the alkyl chain and the EO groups. The distinct peak at 3080  $\text{cm}^{-1}$  is the symmetric C-H stretch of the aromatic ring.

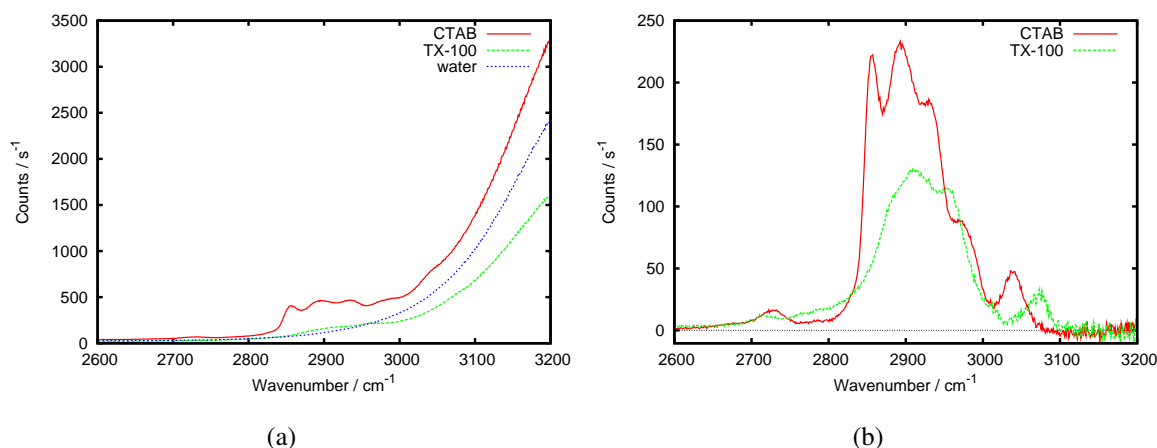


Figure 3: Spectra for CTAB, TX-100 and water. a) Raw spectra; b) Spectra after subtraction of water background. S polarization. Acquisition time = 360 s.

For the kinetics measurements a much shorter acquisition time of 1 s was used, with a 1-s readout time between each measurement limited by the spectrometer software. Figure 4 shows a set of 10 sequential spectra from a kinetics experiment with 3 mM CTAB, illustrating the signal to noise achieved in a 1-s acquisition.

A typical kinetics run would contain 300 spectra starting from before the injection of the surfactant until after the surface had reached equilibrium. Both the equilibrium and kinetic measurements

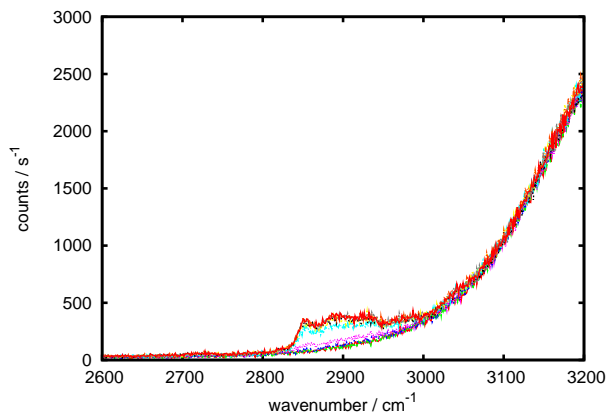


Figure 4: Ten sequential spectra from a kinetics experiment with 3 mM CTAB. 1-s acquisition time, S polarization.

were analyzed using a chemometric method known as target factor analysis (TFA).<sup>26</sup> The first step in TFA is to decompose the data set into its principal components. For the pure surfactants, the first two components contain orthogonal linear combinations of the water and surfactant spectra while the remaining components are noise. The second step is a coordinate rotation to extract the refined spectra corresponding to the water and the surfactant and their component weights in each of the kinetic spectra. To perform this rotation a pair of target spectra are required that approximate to the refined water and refined surfactant spectra. The target spectrum for water was acquired at the beginning of each experiment with pure water in the cell. The target spectrum for the surfactant was obtained by manual subtraction of the water target spectrum from the spectrum of the highest concentration surfactant solution. Figure 5 compares the target spectrum for TX-100 with the refined spectrum obtained from a set of equilibrium spectra at different concentrations and a kinetic spectrum from a single experiment. The differences between the target and refined spectra are very small, though the noise on the refined kinetic spectrum is higher owing to the much shorter acquisition times. The component weight of the surfactant spectrum from the TFA was divided by the component weight of the water spectrum to compensate for any drift in the microscope focus or laser power and to account for differences in the acquisition time (so that the longer equilibrium measurements appeared on the same scale as the brief kinetic measurements).

Target Factor Analysis yields component weights that determine the relative contribution of the

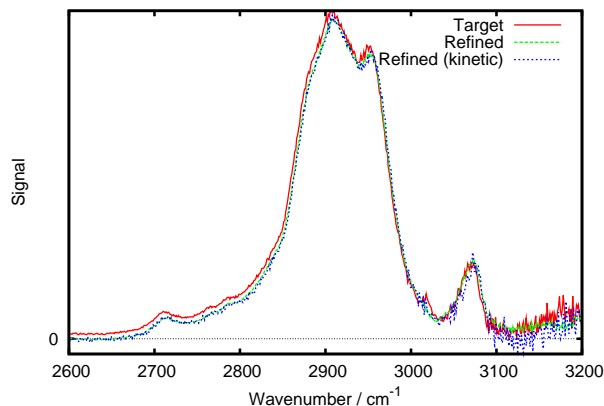


Figure 5: Example of target and refined spectra for TX-100. Two refined spectra are shown: one from the analysis of an equilibrium TX-100 isotherm and one from the analysis of a single kinetic run.

refined spectra to each raw spectrum in the data set. The absolute values of the component weights have no meaning. A calibration procedure is required to convert the component weight of the surfactant into a surface excess (in moles  $\text{m}^{-2}$  of surface). The surface excess was calibrated from the contribution to the equilibrium Raman spectra from surfactants molecules in bulk solution within the evanescent wave: the number of bulk molecules contributing to the signal is simply the bulk concentration multiplied by the sampling depth. Above the cmc of a single surfactant system, the surface excess remains constant and therefore the increase in Raman signal with increasing surfactant concentration may be ascribed to bulk surfactant. So above the cmc, the component weight of the surfactant should be linear in concentration, with a slope that yields a calibration factor to convert component weight into surface excess. This calibration relies on four assumptions: first, that the adsorbed and bulk surfactant have the same spectra; second, that the spread of angles around the incident angle is small enough to be neglected; third, that the bulk concentration is uniform; fourth, that the surfactant is pure. For disordered surfactant layers the first assumption holds well, as does the second provided that the angle of incidence is not too close to the critical angle. The third assumption holds for non-ionic surfactants and for ionic surfactants provided that the Debye length is small compared to the penetration depth. The fourth assumption does not hold for Triton X-100, which is a mixture of isomers and EO chain length; the slope of the isotherm well above

the cmc gives an average calibration factor for the surfactant. The combined error arising from the spread of angles, the error in the measurement of the angle of incidence and the effect of the polydispersity of the surfactant is difficult to estimate precisely, but could be as much as 20%. The absolute surface excesses in this paper should therefore be treated with a degree of caution, while relative surface excesses are much more accurate.

## Wall-jet cell

The sample cell is illustrated in Figure 6. The custom-made glass cell consists of an inner chamber with a volume of 6 mL surrounded by an outer jacket through which temperature-controlled water is passed. A tube allows a thermocouple probe to be inserted into the outer jacket. The top of the sample chamber is capped with a 10-mm diameter silica hemisphere sealed to the chamber with a Viton O-ring. An inlet tube (1-mm inner radius) is positioned 1.8 mm below the hemisphere surface. Most modeling has been done on flow systems comprising a hole in a plate rather than a nozzle, in order to minimize the formation of vortices either side of the nozzle.<sup>27</sup> However, Melville *et al.*<sup>28</sup> showed that the flux at the surface was only  $\sim 2\%$  greater for a submerged nozzle compared to a hole in a plate, and so the difference in flux can be neglected in all but the most precise work. Unless otherwise specified the surfactant solutions were injected at a rate of  $0.5 \text{ mL min}^{-1}$  corresponding to a mean flow rate in the inlet pipe of  $0.27 \text{ mm s}^{-1}$ . The inlet pipe is sufficiently long that parabolic flow is established in the nozzle.

The cell, the tubing connecting the cell, and all the other glassware used in the experiment was cleaned with a commercial alkaline cleaning agent (Borer 15PF concentrate), then rinsed with copious high-purity water. The fused silica hemispheres were cleaned by soaking in chromosulfuric acid for at least 4 hours, then rinsed with high purity water. Between each experiment the cell was flushed with at least 100 mL of high purity water to wash any residual surfactant off the surface. Typically, equilibrium measurements and kinetic measurements were taken back-to-back: the cell was rinsed with water, the surfactant solution was flushed into the cell while the adsorption kinetics were recorded, then once adsorption was complete the longer equilibrium spectra were

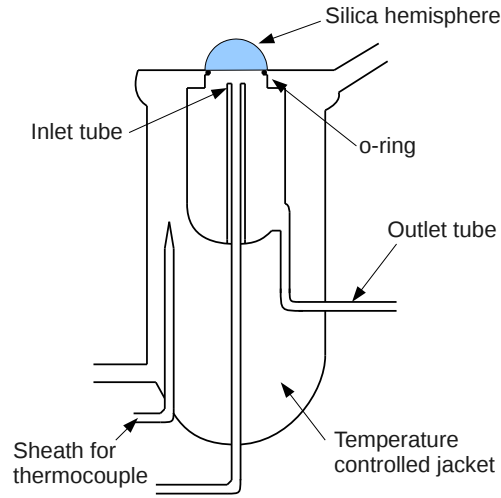


Figure 6: Diagram of the flow cell.

taken. If desorption measurements were also required then the cell was emptied and refilled with the surfactant solution (to ensure that the concentration was correct) before pure water was flushed in while the desorption was measured.

## Modeling

For a single species in an incompressible fluid, the convection-diffusion equation in the bulk solution is

$$\frac{\partial c}{\partial t} - D\nabla^2 c + \mathbf{v} \cdot \nabla c = 0 \quad (1)$$

where  $c$  is the concentration of the species,  $D$  is the mutual diffusion coefficient (using the mutual diffusion coefficient rather than the self diffusion coefficient allows us to neglect the migration term for ionic surfactants) and  $\mathbf{v}$  is the fluid velocity. Near the axis of symmetry (within  $< 20\%$  of the tube radius and height) the fluid velocity in polar coordinates is given by<sup>23</sup>

$$v_r = \alpha z r$$

$$v_z = -\alpha z^2 \quad (2)$$

$$v_\phi = 0$$

The positive  $z$ -direction is defined as the normal from the hemisphere surface towards the solution, with  $z = 0$  at the silica-water interface.  $\alpha$  is a constant that depends on the radius of the nozzle, the height of the nozzle from the surface and the Reynolds number; Dąbroś and van de Ven calculated values of  $\alpha$  for a variety of different parameters.

In order to simplify the convection-diffusion equation, we first non-dimensionalize  $z$  by  $(D/\alpha)^{1/3}$ , (the thickness of the diffusion layer:  $\sim 50 \mu\text{m}$ );  $r$  by the nozzle radius,  $R$  ( $= 1 \text{ mm}$ ); and  $t$  by  $(D\alpha^2)^{-1/3}$  (the time taken to diffuse across the diffusion layer:  $\sim 4 \text{ s}$ ). We will choose the non-dimensionalization for  $c$  later when we identify the boundary conditions at the surface. The convection-diffusion equation becomes (in cylindrical polar coordinates)

$$\frac{\partial c}{\partial t'} - \frac{(D/\alpha)^{2/3}}{R^2 r'} \frac{\partial}{\partial r'} \left( r' \frac{\partial c}{\partial r'} \right) - \frac{\partial^2 c}{\partial z'^2} + z' r' \frac{\partial c}{\partial r'} - z'^2 \frac{\partial c}{\partial z'} = 0 \quad (3)$$

where  $r'$ ,  $t'$  and  $z'$  are the non-dimensionalized coordinates. Since  $(D/\alpha)^{2/3}/R^2 < 10^{-2}$ , we can neglect the second term in Eq. (3). The concentration goes through a maximum at  $r' = 0$ , so we can write  $c(r') \approx c_0(1 - \beta r'^2)$  near  $r = 0$ , and so  $\frac{\partial c}{\partial r'} \approx 2c_0\beta r'$ . Therefore, the fourth term in Eq. (3) scales as  $r'^2$  and hence can be neglected close to the axis (where  $r'$  is small). Thus the convection-diffusion equation reduces to a one-dimensional problem,

$$\frac{\partial c}{\partial t'} - z'^2 \frac{\partial c}{\partial z'} - \frac{\partial^2 c}{\partial z'^2} = 0 \quad (4)$$

To solve Eq. (4) numerically, we first express it in finite difference forms that are backward in time and centered in space:

$$-\left( \frac{1}{\Delta z'^2} - \frac{j^2 \Delta z'}{2} \right) c_{j-1}^n + \left( \frac{2}{\Delta z'^2} + \frac{1}{\Delta t'} \right) c_j^n - \left( \frac{1}{\Delta z'^2} + \frac{j^2 \Delta z'}{2} \right) c_{j+1}^n = \frac{c_j^{n-1}}{\Delta t'} \quad (5)$$

where  $j$  is the index in space (with the surface at  $j = 0$ ) and  $n$  is the index in time.  $\Delta z'$  and  $\Delta t'$  are the step-sizes in non-dimensionalized space and time, respectively.

The convection-diffusion equation can then be expressed in matrix form as

$$\mathbf{d}^{n-1} = \mathbf{T}\mathbf{u}^n \quad (6)$$

where  $\mathbf{d}^{n-1}$  is a vector with elements based on concentration at the previous time-step:  $d_j^{n-1} = c_j^{n-1}/\Delta t'$ , and  $\mathbf{u}^n$  is a vector of concentrations at the current time step. The Thomas (or double-sweep) algorithm<sup>29</sup> is used to invert the matrix and thus calculate the concentrations at the current time step.

## Simple boundary conditions

The boundary condition far from the surface,  $c_{jj}^n$ , is simply the inlet concentration. The boundary conditions at  $t = 0$  depend on the experiment being modeled: for adsorption kinetics the concentration throughout the whole cell is set to 0; for desorption kinetics the concentration throughout the whole cell is set to the bulk concentration prior to rinsing.

The boundary condition applied at the adsorbing surface should be consistent with the equilibrium adsorption isotherms of the surfactant and reflect a physically reasonable model. There are, however, a few simpler models that are worth exploring first.

(i) In the perfect sink model, all molecules that reach the surface adsorb irreversibly. The surfactant concentration in the cell adjacent to the surface is held at 0, and flux to the surface is given by

$$j = D \left. \frac{\partial c}{\partial z} \right|_{z=0} \quad (7)$$

The steady-state solution to the convective diffusion equation with this boundary condition has been evaluated by Dijt *et al.*,<sup>15</sup>

$$j = 0.77646D^{2/3}\alpha^{1/3}c_{\text{in}} \quad (8)$$

The dimensionless constant 0.77646 is equal to  $9^{1/3}/\Gamma(1/3)$ , where  $\Gamma(x)$  is the gamma function<sup>12</sup> (elsewhere we use  $\Gamma$  for the surface excess). Equation (8) has been used extensively to model adsorption kinetics in wall-jets.<sup>15–18</sup> In our experiments, the surface excess saturates well before the flux to the surface reaches its limiting value. Consequently, Eq. (8) is of limited quantitative value.

(ii) If the surfactant does not adsorb at all, then the appropriate boundary condition is one of no flux:

$$\left. \frac{\partial c}{\partial z} \right|_{z=0} = 0 \quad (9)$$

This condition is not useful for monomeric surfactants, but it is useful in solutions above the critical micelle concentration if one makes the conventional (though not necessarily correct<sup>30</sup>) assumption that micelles do not adsorb.

## Adsorption isotherms

The simplest monolayer adsorption isotherm is due to Langmuir:<sup>31</sup>

$$\frac{\Gamma}{\Gamma_\infty} = \frac{K_L c}{1 + K_L c} \quad (10)$$

where  $\Gamma_\infty$  is the number of adsorption sites per unit area and  $K_L$  the Langmuir constant. The Langmuir isotherm does not account for the interactions between adsorbed molecules. An extension due to Frumkin<sup>32</sup> accounts for adsorbate-adsorbate interactions through an interaction parameter,  $\omega$ , within the Bragg-Williams approximation (i.e. random mixing):

$$\frac{\Gamma}{\Gamma_\infty} = \frac{K_L e^{\omega\Gamma/\Gamma_\infty} c}{1 + K_L e^{\omega\Gamma/\Gamma_\infty} c} \quad (11)$$

Following the approach of Curwen *et al.*,<sup>13</sup> we adopt the kinetic scheme

$$\frac{d\Gamma}{dt} = k_a e^{\omega_a\Gamma/\Gamma_\infty} c (\Gamma_\infty - \Gamma) - k_d e^{\omega_d\Gamma/\Gamma_\infty} \Gamma \quad (12)$$

where  $K_L = k_a/k_d$  and  $\omega = \omega_a - \omega_d$ . This scheme is consistent with the equilibrium Frumkin isotherm. As before, we can non-dimensionalize this scheme so that  $\Gamma$  is divided by  $\Gamma_\infty$  and  $c$  by  $\Gamma_\infty(\alpha/D)^{1/3}$ . The latter represents the bulk concentration for which the amount of surfactant in the diffusion layer is equal to the amount in a saturated surface layer. For a typical value of  $\Gamma_\infty = 5 \mu\text{mol m}^{-2}$ ,  $\Gamma_\infty(\alpha/D)^{1/3} \sim 0.1 \text{ mM}$ . The non-dimensionalized form of Eq. (12) is

$$\frac{d\Gamma'}{dt'} = k'_a e^{\omega_a \Gamma'} c'(1 - \Gamma') - k'_d e^{\omega_d \Gamma'} \Gamma' \quad (13)$$

where  $k'_a = \Gamma_\infty(D^2\alpha)^{-1/3}k_a$  and  $k'_d = (D\alpha^2)^{-1/3}k_d$ . Where we have fitted data to obtain constants for the Frumkin model, the dimensional forms are presented.

We split this equation into the finite difference form

$$\Gamma'^{n-1} - \Gamma'^n + \Delta t' k'_a e^{\omega_a \Gamma'^n} c_0'^n (1 - \Gamma'^n) - \Delta t' k'_d e^{\omega_d \Gamma'^n} \Gamma'^n = 0 \quad (14)$$

and create a special case of equation (5) for  $j = 0$ , describing the solution immediately next to the solid surface:

$$\left( \frac{1}{\Delta t'} + \frac{1}{\Delta z'^2} + \frac{k'_a e^{\omega_a \Gamma'^n}}{\Delta z'} (1 - \Gamma'^n) \right) c_0'^n - \frac{1}{\Delta z'^2} c_1'^n = \frac{c_0'^{n-1}}{\Delta t'} + \frac{k'_d e^{\omega_d \Gamma'^n}}{\Delta z'} \Gamma'^n \quad (15)$$

Eq. (15) is nonlinear in  $\Gamma'$  therefore the set of partial differential equations cannot be written in the form of Eq. (6). We circumvent this problem in the following way: (i) the value of  $c_0$  at the previous time-step,  $n - 1$ , is used in equation (14) to calculate an estimate of  $\Gamma'$  at the current time step,  $n$ ; (ii) the backwards finite difference method is applied as before with this estimate in place of  $\Gamma'^n$  in equation (15); (iii) the calculated subsurface concentration,  $c_0'^n$ , is then used to recalculate  $\Gamma'^n$  using equation (14). If the difference between  $\Gamma'^n$  and its initial estimate is greater than 0.01% of  $\Gamma_\infty$ , then the steps (ii) and (iii) of the calculation are reiterated, using  $\Gamma'^n$  as an improved estimate, until the error criterion is met.

Surfactants such as TX-100—where the isotherm approaches a step function—are character-

ized by a large value of  $\omega$ , representing a strong attractive interaction between neighboring adsorbates. When  $\omega > 4$  there is a phase separation within the adsorbed layer. We have based our treatment of phase separation on the work of Ferri and Stebe.<sup>33</sup> The surface excesses in the two coexisting phases are found by solving the equation

$$\int_{a_2}^{a_1} \gamma da = \gamma(a_1 - a_2) \quad (16)$$

where  $a_1$  and  $a_2$  are the area per molecule of the surfactant at the two binodal points (equal to  $1/\Gamma_1$  and  $1/\Gamma_2$  respectively), and the surface free energy,  $\gamma$ , is given by

$$\gamma = \gamma_0 + RT\Gamma_\infty \left[ \ln \left( 1 - \frac{\Gamma}{\Gamma_\infty} \right) + \frac{\omega}{2} \left( \frac{\Gamma}{\Gamma_\infty} \right)^2 \right] \quad (17)$$

$\gamma_0$  is the surface free energy at the pure solvent interface, but cancels out and need not be known for any calculation. We avoid the trivial solution where  $\Gamma_1 = \Gamma_2$ . When the surface excess is below  $\Gamma_1$  or above  $\Gamma_2$  the calculation of concentrations and surface excesses proceeds as described above using equations (14) and (15); when the surface excess is between the two binodal points we use a lever rule, so that

$$\frac{\partial \Gamma'}{\partial t} = (1-x) \left[ k'_a e^{\omega_a \Gamma'_1} c' (1 - \Gamma'_1) - k'_d e^{\omega_d \Gamma'_1} \Gamma'_1 \right] + x \left[ k'_a e^{\omega_a \Gamma'_2} c' (1 - \Gamma'_2) - k'_d e^{\omega_d \Gamma'_2} \Gamma'_2 \right] \quad (18)$$

where  $x$  is the fraction of adsorbed surfactant in the second state, given by

$$x = \frac{\Gamma' - \Gamma'_1}{\Gamma'_2 - \Gamma'_1} \quad (19)$$

## Micelles

At concentrations above the cmc, the surfactant exists as both monomers and micelles. Micelles normally have a lower diffusion coefficient than monomers due to their larger size and therefore mass transport of the micelles must be modeled separately from that of monomers. Following the

example of Curwen *et al.*,<sup>13</sup> we assume that micelles are monodisperse, the diffusion coefficients are concentration independent and the exchange between monomers and micelles is fast on the timescale of the experiment. The mass transport of the surfactant in micelles and as monomer is calculated separately, with a no-flux boundary condition for the micelles, and the concentrations summed at the end of each time step. The total concentration is then repartitioned between micelles and monomers so that the concentration of monomers is capped at the cmc and any remaining surfactant is assigned to the micelles.

## Diffusion coefficients

For TX-100 we used values for the diffusion coefficient,  $D_{\text{mon}} = 2.8 \times 10^{-10} \text{ m}^2 \text{ s}^{-1}$  for monomers<sup>34</sup> and  $D_{\text{mic}} = 0.53 \times 10^{-10} \text{ m}^2 \text{ s}^{-1}$  for micelles.<sup>35</sup> As TX-100 is a non-ionic surfactant the mutual diffusion coefficient in dilute solutions is equal to the self-diffusion coefficient. For CTAB micelles we used a value of  $D_{\text{mic}} = 0.53 \times 10^{-10} \text{ m}^2 \text{ s}^{-1}$  whereas for monomers we used the formula  $D_{\text{mon}} = 2D_{\text{CTA}^+}D_{\text{Br}^-}/(D_{\text{CTA}^+} + D_{\text{Br}^-})$  (with  $D_{\text{CTA}^+} = 5.6 \times 10^{-10} \text{ m}^2 \text{ s}^{-1}$  and  $D_{\text{Br}^-} = 20 \times 10^{-10} \text{ m}^2 \text{ s}^{-1}$ ) to give a mutual diffusion coefficient of  $8.8 \times 10^{-10} \text{ m}^2 \text{ s}^{-1}$  (all CTAB values from Lindman *et al.*<sup>36</sup>).

## Equilibrium Isotherms

We used the CTAB isotherm from Tyrode *et al.*<sup>11</sup> and fitted a Frumkin isotherm (described by equation (11)) to it. Both the original data and the fit are shown in Figure 7. The fit captures the steep rise in the isotherm near the cmc, but the plateau at low surface coverage is not well represented; this plateau arises from electrostatic interactions with surface charges that are not included in the Frumkin model.

The TX-100 isotherm and best fit to the Frumkin model are shown in Figure 8. The experimental isotherm approximates to a step function with a peak at a concentration just above the step. Such peaks are usually attributed to impurities in the surfactant:<sup>21,37</sup> TX-100 is a mixture

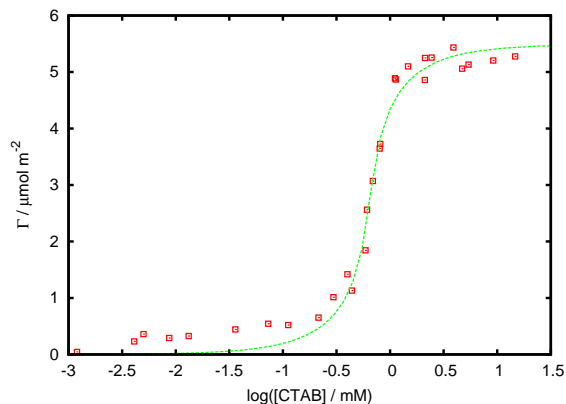


Figure 7: CTAB isotherm (points, taken from ref. 11) and best Frumkin model fit (line,  $\Gamma_\infty = 5.49 \times 10^{-6} \text{ mol m}^{-2}$ ,  $K_L = 0.33 \text{ mol}^{-1} \text{ m}^3$ ,  $\omega = 3.1$ ). The experimental data shown were acquired with an S-polarized pump laser and y-polarized detection. Isotherms obtained with other polarization combinations were very similar.

of different EO chain lengths and isomers of the hydrophobic moiety. We excluded all points with  $\Gamma > 4.8 \mu\text{mol m}^{-2}$  in fitting an isotherm to the data, since no single-component isotherm can account for such a shape. A possible physical interpretation of the step in the isotherm is the coexistence of monomers and aggregates on the surface.

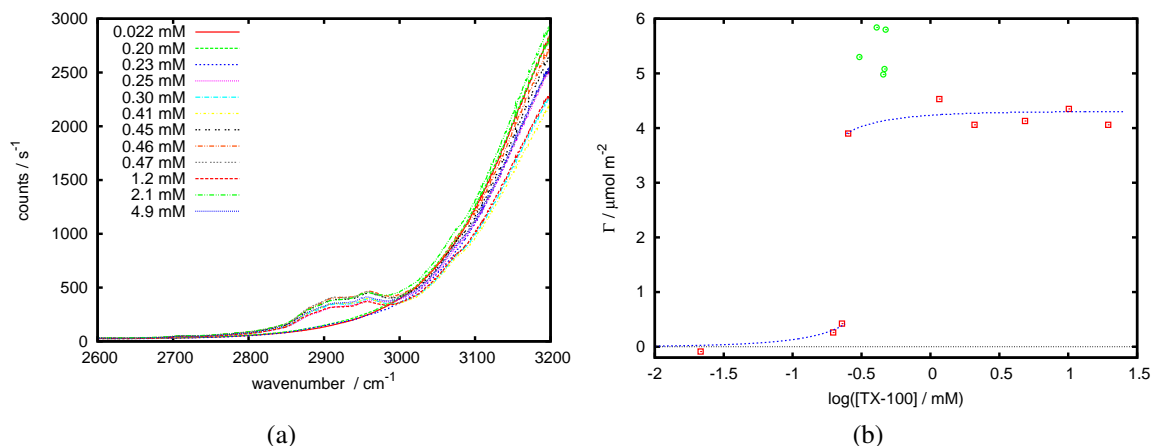


Figure 8: a) Raw spectra used to generate the TX-100 isotherm, and b) the isotherm itself. Circles and squares are both experimental measurements, with the circles being excluded from the fitting process. The lines represent the best fit Frumkin isotherm ( $\Gamma_\infty = 4.30 \times 10^{-6} \text{ mol m}^{-2}$ ,  $K_L = 0.26 \text{ mol}^{-1} \text{ m}^3$ ,  $\omega = 5.5$ ). The discontinuity in the line occurs where there is coexistence between two phases of different surface densities.

The parameters  $K_L$  and  $\omega$  are strongly correlated and acceptable fits could be achieved for a

range of values of  $\omega > 4$ . For fitting the kinetic data we used the best fit value of  $\omega = 5.5$ .

## Kinetics

### CTAB

We recorded the adsorption kinetics of CTAB onto a clean silica surface at concentrations of CTAB from 0.03 to 10 mM at a pumping rate of  $0.5 \text{ mL min}^{-1}$ , for which  $\alpha = 5000 \text{ m}^{-1} \text{ s}^{-1}$  in Eq. (2). We also measured the adsorption kinetics of a 1.2 mM CTAB solution as a function of pumping rate between  $0.12$  and  $1.6 \text{ mL min}^{-1}$ . Figure 9 shows examples of adsorption profiles for 4 surfactant concentrations. Time  $t = 0$  corresponds to the start of the adsorption process; the data are offset to remove the delay between the time when the surfactant was pumped into the flow system and when it reached the surface. The kinetic parameters that provided the best fit to the adsorption curves for the 6 concentrations measured above 0.4 mM are given in the caption. At the lowest concentrations of CTAB ( $< 0.4 \text{ mM}$ ), the equilibrium isotherm underestimates the adsorbed amount and consequently the fit does not match the data (Figure 9 (a) and (b)).

At higher concentrations the fit between experiment and the model is good. The negative values of  $\omega_a$  and  $\omega_d$  shows that both adsorption and desorption become slower at high surface coverage. The former is readily explicable in terms of steric hindrance at high surface coverage. The latter is best thought of as a thermodynamic consequence of the positive value of  $\omega$ , which represents a favorable interaction between neighboring surfactant molecules.

The non-dimensionalized kinetic constants show directly whether the adsorption/desorption rate is limited by mass transport or by kinetic barriers to adsorption or desorption, depending on whether the rate constant is greater or less than unity. For CTAB, the adsorption rate constant  $k'_a e^{(\omega_a \Gamma')}$  varies from 0.6 at low coverage to 0.1 at high coverage, indicating a mixed kinetic / diffusion regime at low coverage and kinetically limited adsorption at high coverage. The desorption rate constant  $k'_d e^{(\omega_d \Gamma')}$  varies from 0.1 at full coverage to 18 at low coverage, the large variation arising from the large negative value of  $\omega_d$ . The initial desorption from the surface is slow and

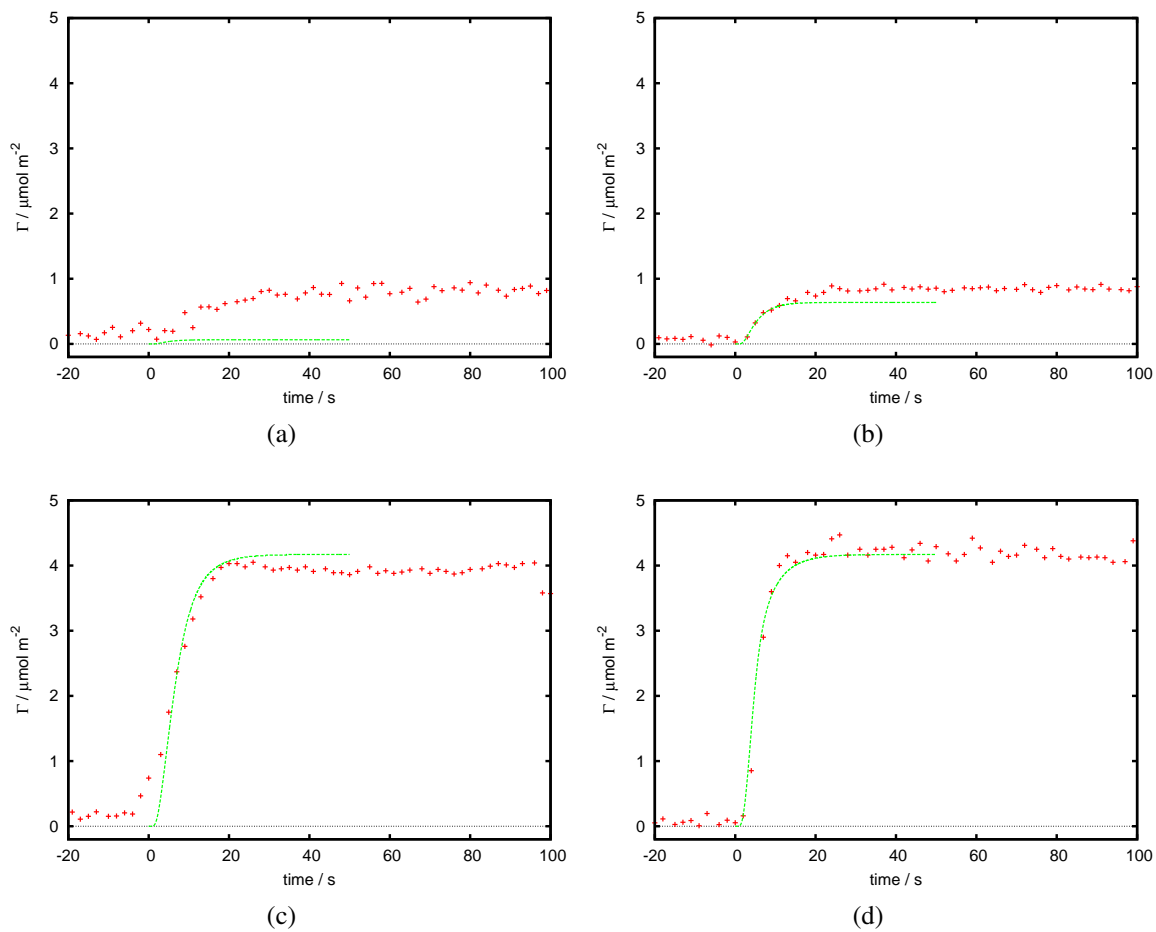


Figure 9: Experimentally measured kinetics (points) and Frumkin model fits (lines) for CTAB adsorbing onto a clean silica surface at concentrations of a) 0.03 mM b) 0.3 mM c) 1 mM d) 3 mM. The fitting parameters used were  $k_a = 1.7 \text{ mol}^{-1} \text{ m}^3 \text{ s}^{-1}$ ,  $k_d = 5 \text{ s}^{-1}$ ,  $\omega_a = -1.9$  and  $\omega_d = -5$ .

kinetically limited, but once the coverage begins to drop the desorption rate accelerates until it becomes mass transport limited.

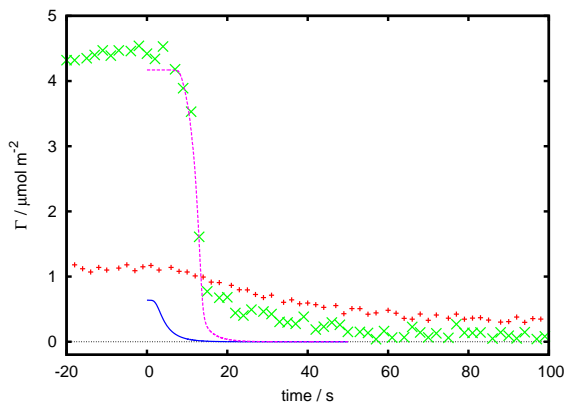


Figure 10: Examples of desorption curves for initial concentrations of 0.3 mM (data: +, model: solid line) and 3 mM (data: ×, model: dashed line). Model parameters taken from Figures (7) & (9).

The kinetics of desorption from surfaces with a high coverage into pure water (e.g. green crosses in Figure 10) are close to diffusion-controlled and therefore rather insensitive to the kinetics at the surface. Nevertheless, it is worthwhile to check how well the desorption kinetics are described by the kinetic parameters calculated from the equilibrium isotherm and the adsorption kinetics. This prediction is shown as the dashed line in Figure 10. The model Frumkin parameters describe the initial desorption kinetics well, but do not fit the long tail in the desorption curve. This disagreement is entirely expected since the Frumkin isotherm does not capture the plateau in the adsorption isotherm of CTAB at low concentrations. For the same reason, the Frumkin parameters provide a very poor fit to the desorption kinetics at the lower initial surface excess.

The sensitivity of the adsorption and desorption curves to the kinetic parameters is illustrated in Figure 11 for a final (adsorption) and initial (desorption) concentration of 3 mM. In each case, the ratio of  $k_a/k_d$ , and the difference  $\omega_a - \omega_d$  were constrained so that  $K$  and  $\omega$  were unchanged.

Figure 12 shows the maximum adsorption rate in experiments where the concentration of CTAB was kept constant at 1.2 mM and the pumping speed varied. The predicted adsorption rates from the kinetic parameters in Figure 9 are shown. Agreement is fair for flow rates of  $< 1 \text{ mL min}^{-1}$ . At higher flow rates the measured rates are lower than predicted, but at these flow

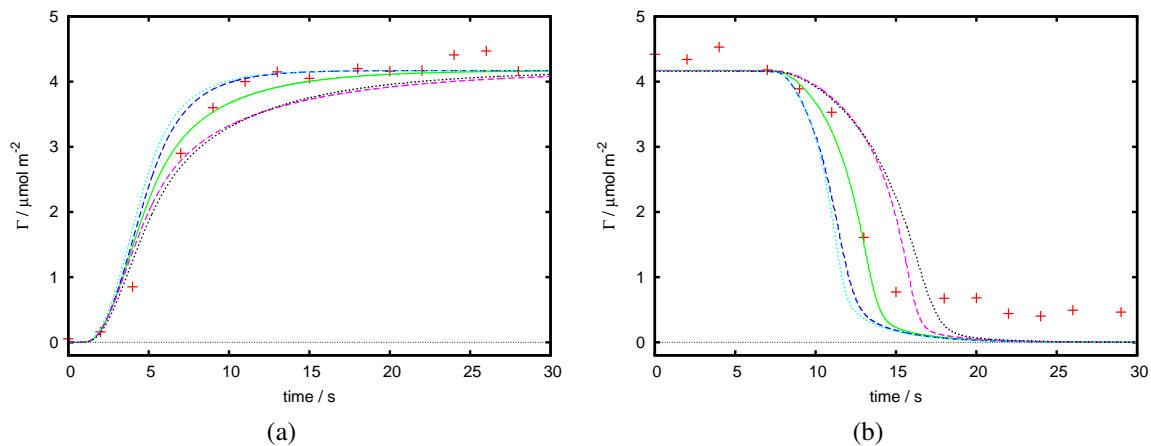


Figure 11: Sensitivity of adsorption and desorption model to changing parameters, shown for 3 mM CTAB. The dashed lines represent a change in  $\omega_a$  and  $\omega_d$  ( $\pm 1$  from the preferred value) whereas the dotted lines represent a change in  $k_a$  and  $k_d$  ( $\times / \div 2$  of the preferred value).

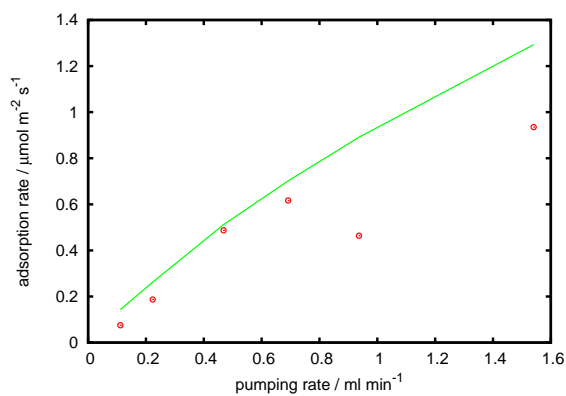


Figure 12: Maximum adsorption rate with respect to surfactant solution (1.2 mM CTAB) injection rate. The solid line is the calculated values while the circles are experimental.

rates we are running into limitations imposed by the sampling frequency of the Raman spectra (0.5 Hz).

## TX-100

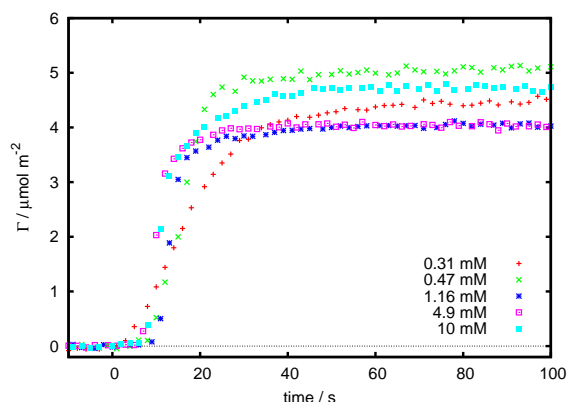


Figure 13: Adsorption of TX-100 at different concentrations.

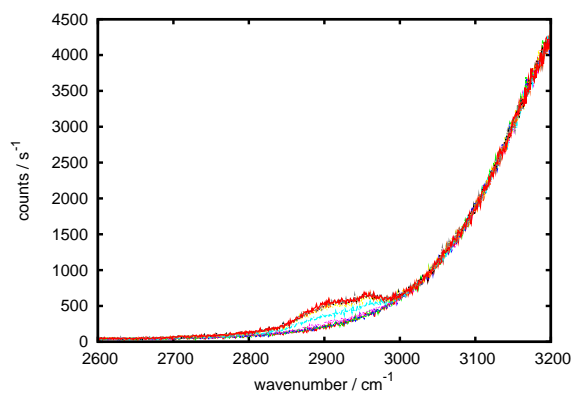


Figure 14: A set of 10 sequential spectra from a TX-100 kinetics experiment (1.16 mM concentration, 1500 mW laser, 1-s acquisition time, S polarization).

The kinetics of adsorption of TX-100 was measured at a range of concentrations from 0.31 to 10 mM, shown in Figure 13. The plateau value at 0.47 mM is elevated compared to the higher concentrations in agreement with the equilibrium isotherm presented in Figure 8. The rise in the plateau at 10 mM arises from the contribution to the signal from bulk surfactant within the evanescent wave. Figure 14 shows a selection of original spectra from one kinetics run to illustrate

the data quality that gives rise to the kinetic plots. The adsorption kinetics of TX-100 were more difficult to model than those of CTAB, even with the addition of the two-phase region of the Frumkin isotherm. The adsorption curves all have a similar shape but with a maximum adsorption rate that increases with increasing bulk concentration.

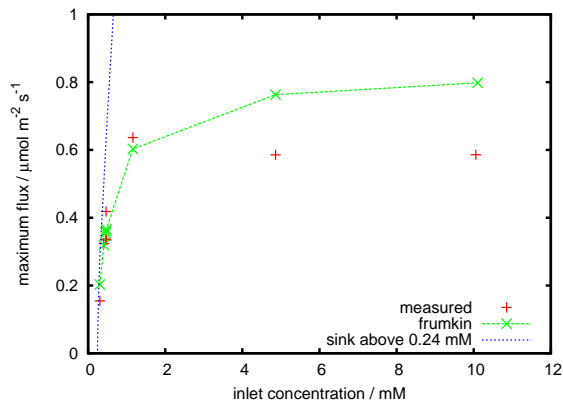


Figure 15: Comparison of experimentally measured (red crosses) and simulated rates of adsorption. The parameters used in the Frumkin simulation are  $k_a = 13 \text{ mol}^{-1} \text{ m}^3 \text{ s}^{-1}$ ,  $k_d = 50 \text{ s}^{-1}$ ,  $\omega_a = -3.5$  and  $\omega_d = -9$ .

Figure 15 compares the experimentally measured maximum rates and calculated rates according to two models. The simpler model uses a no-flux boundary condition for subsurface concentrations below the step in the isotherm at 0.24 mM and perfect sink boundary condition above that concentration. This diffusion-controlled model is in reasonable agreement with the experimental data for concentrations  $< 0.5 \text{ mM}$ . For higher bulk concentrations, the maximum rate of adsorption measured experimentally reaches a plateau indicating that the adsorption rate is limited by interfacial kinetics. Figure 16 shows fits using the Frumkin model on a representative adsorption and desorption curve.

To understand the interplay of kinetic and mass transport limitations, it is helpful to compare the experimental adsorption rates with the maximum adsorption rates from the kinetic model. Since micelles do not adsorb in our model, the maximum adsorption rate is reached when the subsurface concentration is equal to the cmc. The solid red line in Figure 17a shows this kinetically limited flux as a function of surface excess, while the dashed green line shows the flux from the best fit Frumkin parameters for a bulk concentration of 10 mM. This comparison shows that at low

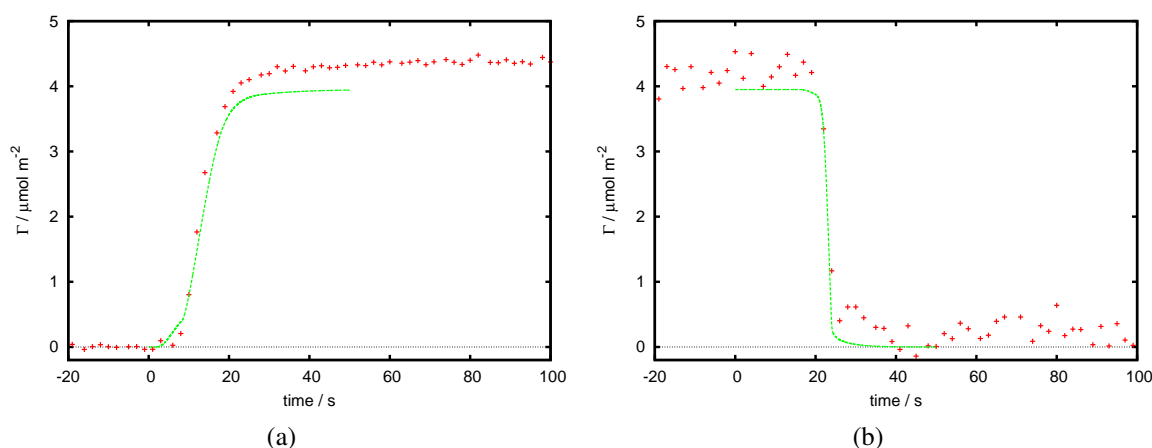


Figure 16: a) Adsorption curve for 0.46 mM TX-100 together with best fit to the Frumkin model (see Fig. 15 for parameters). b) Desorption curve for 2 mM TX-100, and predicted behavior from Frumkin model.

coverages adsorption is mass-transport limited while at higher coverages it is kinetically limited. A similar set of curves is shown in Figure 17b for the desorption of surfactant from the surface when 2 mM TX-100 is replaced by pure water. This comparison shows that the desorption rate is mass-transported limited throughout the whole desorption process. We note that this conclusion cannot be drawn directly from the desorption data in Figure 16, where the measured desorption rate is limited by the sampling speed of the Raman spectrometer.

For TX-100, the Frumkin model gives very different values for the rate constants of adsorption and desorption in the low and high coverage phases. The non-dimensionalized adsorption rate constant decreases from  $\sim 7$  in the low coverage phase to around 0.3 in the high coverage phase, while the desorption rate constant varies even more, from  $> 200$  in the low coverage phase to  $< 0.1$  in the high coverage phase. Thus adsorption to and desorption from the low coverage phase are fast and mass transport limited while in the high coverage phase both processes are kinetically limited. Our model implicitly assumes that the two phases equilibrate rapidly on the surface so the kinetically slow high-coverage phase can desorb rapidly via the labile low-coverage phase once the surface enters the two-phase region. The observed behavior is consistent with this interpretation: once desorption starts it is rapid. We note, however, that we have neglected micellar processes in our model, which may provide alternative mechanisms that explain the experimental data.

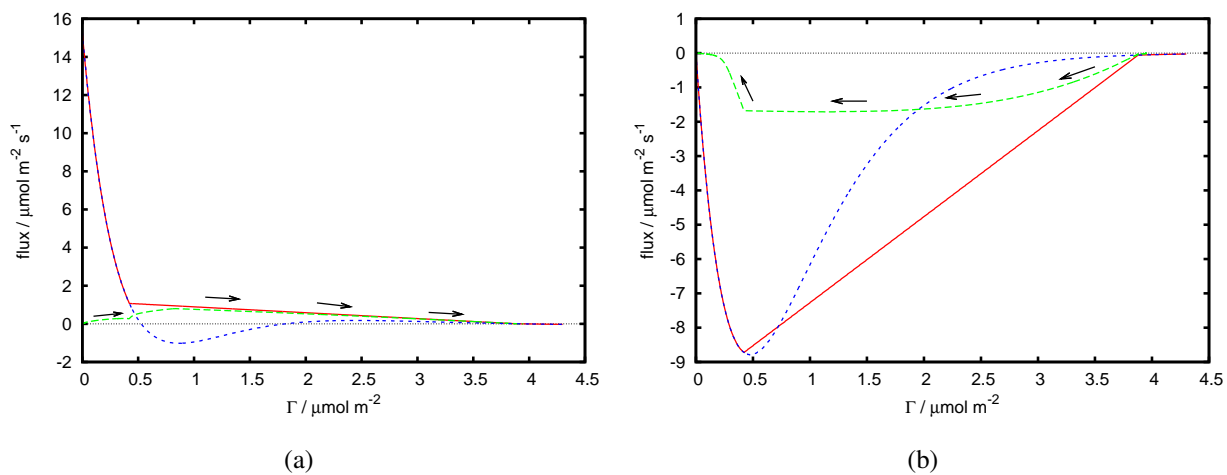


Figure 17: a) Kinetically limited rates of adsorption from the Frumkin model using the preferred fitting parameters and a subsurface concentration equivalent to the cmc. The short-dashed curve (blue) does not account for the phase separation while the solid curve (red) does. The long-dashed curve (green) shows modeled flux during the adsorption of a 10 mM TX-100 solution under experimental conditions; initial rate is limited due to the need for surfactant to diffuse to the surface although later in the process the modeled rate is close to the maximum rate. b) As in a), but showing the kinetically limited rate of desorption when the subsurface concentration is 0. The long-dashed curve (green) shows the modeled flux for the desorption of 2 mM Triton under experimental conditions.

## Comparison with other work

The kinetic parameters determined here can be compared with those in the literature for similar surfactants. Curwen *et al.* used the same kinetic model (though in a cell with different hydrodynamics) to look at the adsorption of the cationic surfactant cetyl pyridinium chloride (CPC) onto a silica surface.<sup>13</sup> In the absence of added electrolyte, the two parameters describing the isotherm on silica ( $K_L$  and  $\omega$ ) are comparable for CPC and CTAB. However, the kinetic parameters differ significantly:  $k_a$  and  $k_d$  are both  $\sim 100\times$  lower for CPC than CTAB, while the values of  $\omega_a$  and  $\omega_d$  are roughly 5 greater for CPC than they are for CTAB. When the combined effect of the two terms is taken into account the difference in rates is less dramatic: at 50% coverage,  $k_a e^{(0.5\omega_a)}$  gives an effective adsorption rate constant of  $0.34 \text{ m}^3 \text{ mol}^{-1} \text{ s}^{-1}$  for CPC and  $0.66 \text{ m}^3 \text{ mol}^{-1} \text{ s}^{-1}$  for CTAB. Similarly,  $k_d e^{(0.5\omega_d)}$  gives an effective desorption rate constant of  $0.20 \text{ s}^{-1}$  for CPC and  $0.41 \text{ s}^{-1}$  for CTAB. The key difference between the two surfactants is not so much the rate as the shape of the adsorption and desorption curves with respect to surface coverage.

Atkin *et al.* also looked at the adsorption of CTAB onto silica (in the form of oxidized silicon).<sup>18</sup> They analyzed their data in terms of “sticking ratio”: the ratio of the maximum measured flux to the surface compared to the maximum possible flux, as given by Eq. (8). In the absence of KCl, they recorded sticking ratios ranging from almost 0, at low concentrations, to 0.2, at or above the cmc (in the presence of KCl the ratios were much higher). For 1 mM CTAB (just above the cmc), the sticking ratio we record is 0.04; almost 5 times lower. This is consistent with the measured fluxes, which are also higher in their work.

Brinck *et al.* studied the adsorption and desorption of non-ionic surfactants  $C_nE_m$  on silica.<sup>38</sup> They used a rather different kinetic model which is not easily compared to the model we employed here. In their model, the majority of the material adsorbing is assumed to consist of aggregates, with transport of aggregates onto the surface assumed to be diffusion-controlled. Monomers could also adsorb to the surface through a process of merging with the adsorbed micelles with a rate constant identical to that of merging with micelles in the bulk. In their model, surfactant adsorption is dominated by micelles due to the very low cmcs of the  $C_nE_m$  surfactants studied (and hence low

monomer concentrations); a situation that does not apply here. The principle advantage of the wall-jet geometry compared to the stirred cuvette used by Brinck *et al.* is that the thickness of the stagnant layer is well-defined and known for the wall jet, whereas for the stirred cuvette the thickness of the stagnant layer must be inferred from the desorption kinetics, which provides no way to deconvolute mass transport effects from the desorption process.

## Conclusions

In this paper we have shown that TIR Raman scattering is a viable method for the study of surfactant adsorption kinetics at the solid–liquid interface. Table 1 compares TIR Raman scattering to some of the other techniques that have been used to study surfactant adsorption kinetics. TIR Raman is competitive with optical reflectometry and ellipsometry in terms of sensitivity but not sampling rate. For the present TIR-Raman study the sampling rates achieved were sufficient under most conditions, though a faster acquisition rate would have been useful for some of the desorption experiments. The key advantage of TIR Raman over reflectometry is the chemical selectivity of the Raman spectroscopy, which is demonstrated in the following paper. The related spectroscopic technique of ATR-IR has comparable performance in terms of the sampling frequency and noise, but it has additional complications that are not present for Raman: water is very IR-active, forcing the use of either D<sub>2</sub>O or deuterated surfactant to avoid overlap with the water peak; much larger sampling areas are required, which presents problems controlling the hydrodynamics over the whole sampled area, and the interpretation of the data is more complex due to the variable penetration depth across the spectrum. The restriction of ATR-IR to infrared-transparent substrates is rather more restrictive than for TIR-Raman which only requires the substrate to be transparent near the wavelength of the excitation laser.

For both CTAB and TX-100, fitting to the Frumkin isotherm yields a positive interaction parameter,  $\omega$ , indicating a strong interaction between neighboring molecules on the surface. For both surfactants the interaction parameters ( $\omega_a$  and  $\omega_d$ ) in the kinetic expressions are negative, show-

**Table 1: Comparison of the limitations of experimental techniques used to study surfactant adsorption kinetics.**

Technique	Sampling frequency / Hz	Typical point-to-point variation (standard deviation)	Comments	Reference
TIR-Raman	0.5	1-5%	Non-fluorescent materials	This work
Ellipsometry / optical reflectometry	Up to 1000	10% at 1kHz; 1% at 1Hz	No chemical selectivity	Curwen <i>et al.</i> <sup>13,14</sup>
ATR-IR	Up to 0.5	1% at 1 Hz	Large sampling areas are needed for short time resolution	Clark and Ducker <sup>6</sup>
QCM	Up to 200	0.3% at 0.2 Hz; 1% at 1 Hz	Water trapped in the adsorbed surfactant layer complicates interpretation of data; no chemical selectivity.	Q-Sense <sup>39</sup>

ing that the rate constants of adsorption and desorption decrease with increasing surface coverage. The negative value of  $\omega_d$  is consistent with the favorable interchain interactions, while the negative value of  $\omega_a$  may arise from the steric hindrance to adsorption at high surface coverage. The non-dimensionalized values of the rate constants indicate whether adsorption is under kinetic or diffusion control. The large and negative values of  $\omega_a$  and  $\omega_d$  result in a strong coverage dependence in the kinetic constants and a change from diffusion control at low surface coverages to a kinetically controlled or mixed regime at high coverages.

The methodology we present here for studying adsorption kinetics is general and robust. The kinetic parameters are determined from the equilibrium isotherm and the adsorption kinetics alone and the resulting desorption profiles are then predicted with no free parameters. The predicted and measured desorption profiles are in good agreement except in regions of low coverage of CTAB where the Frumkin isotherm fails to represent the adsorption isotherm of CTAB adequately.

## References

- (1) Kissa, E. *Textile Research Journal* **1996**, *66*, 660–668.

- (2) Basu, S.; Luthra, J.; Nigam, K. D. P. *Journal of Environmental Science and Health, Part B: Pesticides, Food Contaminants, and Agricultural Wastes* **2002**, *37*, 331–344.
- (3) Beattie, D.; Lidström Larsson, M.; Holmgren, A. R. *Vibrational Spectroscopy* **2006**, *41*, 198–204, 6th Australian Conference on Vibrational Spectroscopy.
- (4) Chen, N.; Bhushan, B. *Journal of Microscopy* **2006**, *221*, 203–215.
- (5) Alexander, C.; Erdogan, G. *Mixed Surfactant Systems*; American Chemical Society, 1992; Chapter 25, pp 354–365.
- (6) Clark, S. C.; Ducker, W. A. *The Journal of Physical Chemistry B* **2003**, *107*, 9011–9021.
- (7) Thomas, R. *Annual Review of Physical Chemistry* **2004**, *55*, 391–426.
- (8) (a) Fragneto, G.; Lu, J. R.; McDermott, D. C.; Thomas, R. K.; Rennie, A. R.; Gallagher, P. D.; Satija, S. K. *Langmuir* **1996**, *12*, 477–486; (b) Penfold, J.; Tucker, I.; Thomas, R. K. *Langmuir* **2005**, *21*, 11757–11764.
- (9) Ikeshoji, T.; Ono, Y.; Mizuno, T. *Appl. Opt.* **1973**, *12*, 2236–2237.
- (10) (a) Beattie, D. A.; Winget, S.; Bain, C. D. *Tribology Letters* **2007**, *27*, 159–167; (b) Lee, C.; Bain, C. D. *Biochimica et Biophysica Acta (BBA) - Biomembranes* **2005**, *1711*, 59–71; (c) Nickolov, Z. S.; Earnshaw, J. C.; McGarvey, J. J. *Journal of Raman Spectroscopy* **1993**, *24*, 411–416; (d) Fujiwara, K.; Watarai, H. *Langmuir* **2003**, *19*, 2658–2664; (e) Ishizaki, F.; Kim, M. *Japanese Journal of Applied Physics* **2008**, *47*, 1621–1627.
- (11) Tyrode, E.; Rutland, M. W.; Bain, C. D. *Journal of the American Chemical Society* **2008**, *130*, 17434–17445.
- (12) Bijsterbosch, H. D.; Cohen Stuart, M. A.; FLeer, G. J. *Macromolecules* **1998**, *31*, 9281–9294.
- (13) Curwen, T. D.; Warner, J. A.; Bain, C. D.; Compton, R. G.; Eve, J. K. *Journal of Physical Chemistry C* **2007**, *111*, 12289–12304.

- (14) Curwen, T. D.; Bain, C. D.; Eve, J. K. *Journal of Physical Chemistry C* **2007**, *111*, 12305–12314.
- (15) Dijt, J. C.; Cohen Stuart, M. A.; Hofman, J. E.; Fleer, G. J. *Colloids and Surfaces* **1990**, *51*, 141–158.
- (16) Torn, L. H.; Koopal, L. K.; de Keizer, A.; Lyklema, J. *Langmuir* **2005**, *21*, 7768–7775.
- (17) Atkin, R.; Craig, V. S. J.; Biggs, S. *Langmuir* **2000**, *16*, 9374–9380.
- (18) Atkin, R.; Craig, V. S. J.; Wanless, E. J.; Biggs, S. *Journal of Colloid and Interface Science* **2003**, *266*, 236–244.
- (19) Rees, N. V.; Klymenko, O. V.; Coles, B. A.; Compton, R. G. *The Journal of Physical Chemistry B* **2003**, *107*, 13649–13660.
- (20) Postmus, B. R.; Leermakers, F. A. M.; Koopal, L. K.; Cohen Stuart, M. A. *Langmuir* **2007**, *23*, 5532–5540.
- (21) Velegol, S. B.; Fleming, B. D.; Biggs, S.; Wanless, E. J.; Tilton, R. D. *Langmuir* **2000**, *16*, 2548–2556.
- (22) Sakai, K.; Smith, E.; Webber, G.; Schatz, C.; Wanless, E.; Butun, V.; Armes, S.; Biggs, S. *Journal of Physical Chemistry B* **2006**, *110*, 14744–14753.
- (23) Dąbroś, T.; van de Ven, T. G. M. *Colloid & Interface Science* **1983**, *261*, 694–707.
- (24) Snyder, R. G.; Strauss, H. L.; Elliger, C. A. *The Journal of Physical Chemistry* **1982**, *86*, 5145–5150.
- (25) O’Leary, T. J.; Levin, I. W. *The Journal of Physical Chemistry* **1984**, *88*, 1790–1796.
- (26) Malinowski, E. R. *Factor Analysis in Chemistry*, 2nd ed.; John Wiley & Sons, 1991.
- (27) Deshpande, M. D.; Vaishnav, R. N. *J. Fluid Mech.* **1982**, *114*, 213–236.

- (28) Melville, J. L.; Simjee, N.; Unwin, P. R.; Coles, B. A.; Compton, R. G. *J. Phys. Chem. B* **2002**, *106*, 10424–10431.
- (29) Abbott, M. B.; R., B. D. *Computational Fluid Dynamics: An Introduction for Engineers*; Longman Scientific & Technical, 1989.
- (30) Colegate, D. M.; Bain, C. D. *Phys. Rev. Lett.* **2005**, *95*, 198302.
- (31) Langmuir, I. *Journal of the American Chemical Society* **1916**, *38*, 2221–2295.
- (32) Frumkin, A. *Zeitschrift für Physik A Hadrons and Nuclei* **1926**, *35*, 792–802.
- (33) Ferri, J. K.; Stebe, K. J. *Journal of Colloid and Interface Science* **1999**, *209*, 1–9.
- (34) Gharibi, H.; Javadian, S.; Sohrabi, B.; Behjatmanesh, R. *Journal of Colloid and Interface Science* **2005**, *285*, 351–359.
- (35) Fang, X. W.; Zhao, S.; Mao, S. Z.; Yu, J. Y.; Du, Y. *Colloid & Polymer Science* **2003**, *281*, 455–560.
- (36) Lindman, B.; Puyal, M. C.; Kamenka, N.; Rymden, R.; Stilbs, P. *The Journal of Physical Chemistry* **1984**, *88*, 5048–5057.
- (37) Trogus, F. J.; Schechter, R. S.; Wade, W. H. *Journal of Colloid and Interface Science* **1979**, *70*, 293–305.
- (38) Brinck, J.; Jonsson, B.; Tiberg, F. *Langmuir* **1998**, *14*, 1058–1071.
- (39) Q-Sense Instruments, [http://www.q-sense.com/qcm\\_d\\_faq--33.asp](http://www.q-sense.com/qcm_d_faq--33.asp) accessed Novemeber 2010.

# Graphical TOC Entry

